

Modelling and analysis of a backward bent duct buoy WEC for oceanographic applications

Ana Paula de Almeida Duarte
ana.a.duarte@tecnico.ulisboa.pt

Instituto Superior Técnico, Universidade de Lisboa, Portugal

June 2018

Abstract

The present thesis was developed within the framework of the WAVEBUOY project, funded by the Portuguese Science and Technology Foundation (FCT). The project aims to design and deploy, for the first time and in the deep ocean, a new generation of general-purpose self-powered oceanographic buoys for data acquisition and long-term ocean observations. The main purpose of this thesis was the development of a new time domain numerical model, to simulate the response of a generic oscillating water column wave energy converter with four degrees of freedom. The model, implemented in OpenModelica, is able to represent the non-linearities of the biradial air turbine and the fully non-linear compressibility of the air chamber. Aiming to understand the influence of the variation of the geometry parameters on the performance of the WAVEBUOY, a sensitivity analysis was carried out in a simplified backward bent duct buoy. It was observed that buoys with a smaller width, a greater duct's transversal area and a certain duct extension performed better than the reference buoy geometry. The performance of the WAVEBUOY was evaluated, using the numerical model. In order to improve its power output and availability, two additional WAVEBUOYs with extended ducts were evaluated. Variations were also made to the turbine rotor diameter and the air chamber's height. It was observed that a WAVEBUOY with a duct extension of 1 m, air chamber with a height of 2.80 m and a turbine rotor diameter of 0.25 m showed a great improvement on the performance and power availability.

Keywords: Wave energy, Oscillating water column, Backward bent duct buoy, Oceanographic applications, Numerical modelling

1. Introduction

1.1. Backward bent duct buoy

The Backward bent duct buoy (BBDB) consists of an L-shaped duct, an air chamber, an air turbine, a generator and a buoyancy module. The wave energy is captured by the surging, heaving and pitching motion of the BBDB and the heaving motion of the oscillating water column (OWC) [1]. The incident waves force the free surface of the wave column to oscillate causing the air inside the chamber to compress and decompress, producing a bidirectional flow through the air turbine that drives a generator and produces electricity.

1.2. WAVEBUOY

The WAVEBUOY, shown in Figure 1, is a small scale BBDB being developed by the IST Wave Energy Group to be deployed in the Condor seamount, Azores. It is meant to be a self-powered oceanographic buoy for data acquisition under long-term deployment periods that requires less maintenance than current alternatives. The device is intended

to extract energy from the waves, generating small amounts of electrical energy to feed oceanographic instrumentation and provide continuous real-time data measurements for ocean monitoring. It has a length of 4 m, a height of 4 m and a width of 3 m, approximately. The device is equipped with a biradial air turbine.

2. Numerical model of a BBDB

A numerical model was developed to simulate the response of a generic floating OWC with four degrees of freedom, three associated to the physical body and one associated to the oscillating water column. The numerical model was based on linear wave theory, therefore small wave amplitudes and body motions were considered. The whole system is required to be modelled as non-linear, due to the fully non-linear compressibility formulation for the air chamber in conjunction with the non-linear flow rate versus pressure drop characteristic of the biradial turbine, and so a time-domain approach is needed. The model is divided in eight sub-models,

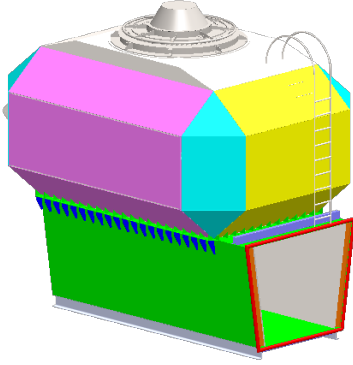


Figure 1: WAVEBUOY designed in SolidWorks by the IST Wave Energy Group team.

as shown in Figure 2: wave forces and moments, buoy & OWC, air chamber, turbine, atmosphere, inertia of rotating masses, generator and batteries. The numerical model consists of employing energy balances in each sub-model, and in those involving fluid, also apply mass balances.

The classical model of a OWC WEC can be seen as the group of buoy & OWC, air chamber and PTO. The turbine, inertia and generator are usually called the PTO. For the sake of simplicity of code implementation, wave forces and moments and buoy & OWC were grouped in a single sub-model denoted as “Waves, buoy and OWC”. The batteries were not included in the present numerical model.

The numerical model was implemented in OpenModelica, an object-oriented language developed for the modelling of large, complex and heterogeneous physical systems.

2.1. Waves, buoy and OWC

Here, the BBDB (duct and buoyancy module) was denoted as body 1. The interior water free surface of the OWC was modelled as an imaginary small thickness rigid piston with density equal to the water density and was denoted as body 2. In this case, the rigid piston should be a good approximation since the dimensions of the OWC free-surface are much smaller than the incident wavelength.

Let x_i be the coordinates of the bodies in the i -th mode, with $x_i = 0$ at equilibrium position. Assuming that body 1 has three modes of movement in surge, heave and pitch, $i \in \{1, 3, 5\}$, and that body 2 has only one mode of movement in heave, $i = 9$, the equations of motion can be written in matrix form as [2]

$$(\mathbf{M} + \mathbf{A})\ddot{\mathbf{X}}(t) = \mathbf{F}^{\text{exc}}(t) - \mathbf{C}^{\text{rest}}\dot{\mathbf{X}}(t) - \mathbf{F}^{\text{rad}}(t) + \mathbf{F}^{\text{press}}(t). \quad (1)$$

Here, the dots denote time derivatives. The left-hand side expression comprises the inertia matrix

\mathbf{M} , the matrix of the limiting values at infinite frequency of the added mass \mathbf{A} and the displacement vector \mathbf{X} , which are given by [2]

$$\mathbf{M} = \begin{pmatrix} m_1 & 0 & m_1 z_g & 0 \\ 0 & m_1 & -m_1 x_g & 0 \\ m_1 z_g & -m_1 x_g & I_{yy} & 0 \\ 0 & 0 & 0 & m_2 \end{pmatrix}, \quad (2)$$

$$\mathbf{A} = \begin{pmatrix} A_{11}^{\infty} & A_{13}^{\infty} & A_{15}^{\infty} & A_{19}^{\infty} \\ A_{31}^{\infty} & A_{33}^{\infty} & A_{35}^{\infty} & A_{39}^{\infty} \\ A_{51}^{\infty} & A_{53}^{\infty} & I_{55}^{\infty} & A_{59}^{\infty} \\ A_{91}^{\infty} & A_{93}^{\infty} & A_{95}^{\infty} & A_{99}^{\infty} \end{pmatrix}, \quad (3)$$

$$\mathbf{X}(t) = \begin{pmatrix} x_1(t) \\ x_3(t) \\ x_5(t) \\ x_9(t) \end{pmatrix}, \quad (4)$$

where the mass of the buoy and piston are denoted as m_1 and m_2 , respectively. The coordinates of the centre of gravity are given by (x_g, y_g, z_g) . The pitching moment of inertia is defined as I_{yy} . The limiting value at infinite frequency of the added mass coefficient is defined as $A_{ij}^{\infty} = \lim_{\omega \rightarrow \infty} A_{ij}(\omega)$ and is obtained using WAMIT.

The right-hand side expression comprises the forces acting on the system, namely the wave excitation force \mathbf{F}^{exc} , the hydrostatic force $\mathbf{C}^{\text{rest}}\mathbf{X}$, the radiation force \mathbf{F}^{rad} and the pressure force that is exerted in the buoy and in the OWC $\mathbf{F}^{\text{press}}$.

The excitation force is represented in matrix form as [2]

$$\mathbf{F}^{\text{exc}}(t) = \begin{pmatrix} F_1^{\text{exc}}(t) \\ F_3^{\text{exc}}(t) \\ F_5^{\text{exc}}(t) \\ F_9^{\text{exc}}(t) \end{pmatrix}, \quad (5)$$

where F_i^{exc} was obtained as a superposition of N angular frequency components ω_m [3]

$$F_i^{\text{exc}} = \sum_{m=1}^N \Gamma_i(\omega_m) A_m \cos(\omega_m t + \phi_{i,m} + \phi_r), \quad (6)$$

where m is the index of each component, $\Gamma_i(\omega_m)$ is the excitation force coefficient of the i -th mode, A_m is the frequency-dependent wave amplitude, $\phi_{i,m}$ is the phase response of the i -th mode at the angular frequency ω_m and ϕ_r is a random phase distributed over the interval $[0, 2\pi]$. Both the excitation force coefficient and the phase response are computed by WAMIT. The wave amplitude is function of the spectral density $S_{\omega}(\omega_m)$ [4]

$$A_m = \sqrt{2\Delta\omega_m S_{\omega}(\omega_m)} \quad (7)$$

The spectral distribution is expressed by the Pierson-Moskowitz spectrum, which is the spectrum that most closely matches the wave resource

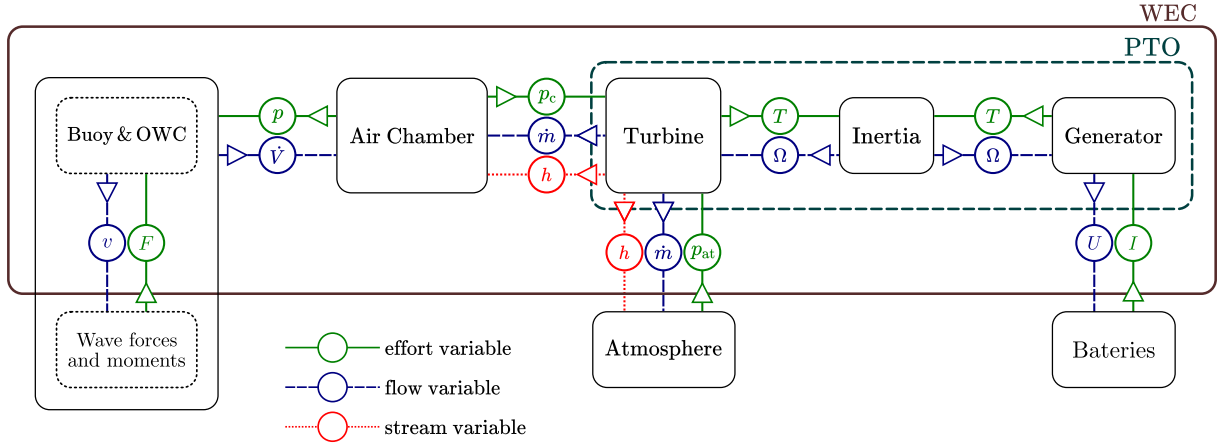


Figure 2: Representation of the structure of the numerical model, showing the interaction variables between all sub-models. The direction of the arrows defines which sub-model sets the variable.

at the buoy deployment location [5],

$$S_\omega(\omega) = \frac{262.9H_s^2}{T_e^4\omega^5} \exp\left(\frac{-1054}{T_e^4\omega^4}\right), \quad (8)$$

where H_s is the significant wave height and T_e is the energy period, which is defined as $T_e \approx 0.857T_p$ [5], where T_p is the peak period. The average flux of energy \bar{P}_{wave} transported by the waves of a sea state described by a Pierson-Moskowitz spectrum in deep water is given by $\bar{P}_{\text{wave}} = 0.490H_s^2T_e$ [kW/m] [5]. The annual average flux of energy transported by the waves $\bar{P}_{\text{wave,ann}}$ in the Condor seamount in Azores is 40.05 kW/m [6].

The annual wave climate has been approximated by a set of 16 sea states, whose characteristics are presented in Table 1. These characteristics include significant wave height, peak period and probability of occurrence μ .

The hydrostatic force is represented in the time domain as a function proportional to the body displacement [2],

$$\mathbf{F}^{\text{hydro}}(t) = \mathbf{C}^{\text{rest}} \mathbf{X}(t) \quad (9)$$

where \mathbf{C}^{rest} represents the matrix of hydrostatic restoring coefficients,

$$\mathbf{C}^{\text{rest}} = \begin{pmatrix} C_{11}^m & 0 & 0 & 0 \\ 0 & C_{33} & C_{35} & 0 \\ 0 & C_{53} & C_{55} & 0 \\ 0 & 0 & 0 & C_{99} \end{pmatrix}, \quad (10)$$

whose non-zero elements are [5]

$$\begin{cases} C_{33} = \rho_w g S_1, \\ C_{35} = C_{53} = -\rho_w g S_x, \\ C_{55} = \rho_w g S_{xx} + \rho_w g V_b z_b - m_b g z_g, \\ C_{99} = \rho_w g S_2. \end{cases} \quad (11)$$

Table 1: Characteristic wave climate in the Condor seamount, in Azores. Each sea state n of the wave climate is defined by H_s , T_p and μ . Retrieved from [6].

n	H_s [m]	T_p [s]	μ [%]
1	2.06	10.60	24.79
2	2.21	12.60	12.34
3	1.97	8.45	10.93
4	3.36	12.80	9.59
5	1.10	8.45	7.07
6	3.30	10.80	6.94
7	5.38	13.00	5.98
8	1.14	10.30	5.65
9	5.81	14.80	2.57
10	4.89	10.90	2.47
11	3.25	8.46	2.10
12	2.12	15.00	2.08
13	2.02	6.40	1.99
14	3.41	14.70	1.96
15	1.11	12.80	1.90
16	1.07	15.80	1.62

The surge mode is considered neutrally stable, being the reason why there is no hydrostatic restoring effect observed for that mode. When necessary, external forces, like mooring lines for example, provide the restoring effect, which is the case. In order to avoid drift in surge mode, it is assumed to exist a mooring line modelled as a spring with stiffness C_{11}^m . In equation (11), ρ_w is the fluid density, V_b is the static volume, which is the volume of fluid displaced by the floating body in a fixed position, g is the acceleration of gravity, (x_b, y_b, z_b) are the coordinates of the centre of buoyancy, S_1 and S_2 are the body waterplane areas of bodies 1 and 2, respectively, and S_x and S_{xx} are waterplane mo-

ments.

The radiation force is represented in the time domain through a convolution integral [7],

$$\mathbf{F}^{\text{rad}}(t) = \int_0^t \mathbf{K}(t - \tau) \dot{\mathbf{X}} d\tau, \quad (12)$$

where \mathbf{K} is the matrix of the impulse response functions (IRFs) associated with the convolution integral

$$\mathbf{K} = \begin{pmatrix} K_{11}(t) & K_{13}(t) & K_{15}(t) & K_{19}(t) \\ K_{31}(t) & K_{33}(t) & K_{35}(t) & K_{39}(t) \\ K_{51}(t) & K_{53}(t) & K_{55}(t) & K_{59}(t) \\ K_{91}(t) & K_{93}(t) & K_{95}(t) & K_{99}(t) \end{pmatrix}. \quad (13)$$

The convolution integrals present in \mathbf{F}^{rad} were approximated by a state-space formulation of order n , which consists of representing the convolution integral by a small number of first order linear differential equations with constant coefficients. The state-space representation is expressed by

$$\dot{\mathbf{y}}_{ij} = \mathbf{A}_{ij}^r \mathbf{y}_{ij} + \mathbf{B}_{ij}^r \dot{x}_j \quad (14)$$

$$F_{ij}^{\text{rad}} = \mathbf{C}_{ij}^r \mathbf{y}_{ij} \quad (15)$$

where the constant coefficient matrix $\mathbf{A}_{ij}^r \in \mathbb{R}^{n \times n}$ and vectors $\mathbf{B}_{ij}^r \in \mathbb{R}^{n \times 1}$ and $\mathbf{C}_{ij}^r \in \mathbb{R}^{1 \times n}$ define the state-space realization and $\mathbf{y}_{ij} \in \mathbb{R}^{n \times 1}$ represents the state vector, which summarizes the past information of the system at any time instant [7, 8]. The constant coefficients of the differential equations, i.e. \mathbf{A}_{ij}^r , \mathbf{B}_{ij}^r and \mathbf{C}_{ij}^r , were obtained using BEMIO [8], which is a code developed to process output files from WAMIT and that calculates state-space realization coefficients through those WAMIT outputs. This approximation requires lower computation resources than direct numerical integration, because the calculation of the convolution integral at each time step is avoided [9].

The pressure force that is exerted in the buoy and in the OWC is defined as [2]

$$\mathbf{F}^{\text{press}} = \begin{pmatrix} 0 \\ (p - p_{\text{at}})S_2 \\ 0 \\ -(p - p_{\text{at}})S_2 \end{pmatrix}. \quad (16)$$

where p the instantaneous absolute pressure inside the air chamber and p_{at} is the atmospheric pressure.

The air volumetric flow rate that serves as input to the air chamber is defined as

$$\dot{V} = -(\dot{x}_3 - \dot{x}_9)S_2. \quad (17)$$

2.2. Air chamber

The air chamber is delimited by the water interior free surface, the BBDB walls and the turbine inlet. The air chamber together with its connection to

the atmosphere through the air turbine form a control volume, which is subject to a thermodynamic process of compression and expansion. Considering that the amount of heat transferred across the system's walls is small compared to the amount of work done by the motion of the piston, the process may be considered as approximately adiabatic. In the current model, the gas behaves as an ideal gas and follows the equation of state

$$p = \rho RT, \quad (18)$$

where ρ is the density, R is the constant for the particular gas and T is the temperature.

During the compression process, the specific entropy of the air inside the chamber does not change since the heat transfer through the walls and the viscous losses are considered to be negligible. In the expansion process, the flow that comes from the atmosphere passing through a turbine with losses has a different specific entropy from the air inside the chamber. Since the system is open, the air temperature inside the chamber is not constant and has relatively small amplitude variation.

The principle of mass conservation applied to the air chamber control volume is given by

$$\frac{dm}{dt} = -\dot{m}_{\text{turb}}, \quad (19)$$

where dm/dt is the time rate of change of mass m within the control volume. The mass flow rate through the turbine is denoted as \dot{m}_{turb} and is positive for outward flow and negative on inward flow.

The principle of energy conservation applied to the air chamber, assuming negligible kinetic and potential energy changes inside the chamber during operation, is given by

$$\frac{dU}{dt} = \begin{cases} -\dot{m}_{\text{turb}}h_c - p\dot{V}, & \text{if } p \geq p_{\text{at}} \\ & \text{(exhalation)} \\ -\dot{m}_{\text{turb}}h_{\text{turb}}^{\text{out}} - p\dot{V}, & \text{if } p < p_{\text{at}} \\ & \text{(inhalation)} \end{cases}, \quad (20)$$

where h_c and $h_{\text{turb}}^{\text{out}}$ represent the specific enthalpy at the air chamber's outlet and turbine's outlet, respectively. In the air chamber there is no external work done on the fluid.

2.3. Turbine

The performance characteristics of the turbine are presented in dimensionless form, as follows [3]

$$\Psi = \frac{p - p_{\text{at}}}{\rho_{\text{in}} \Omega^2 d^2}, \quad (21)$$

$$\Phi = \frac{\dot{m}_{\text{turb}}}{\rho_{\text{in}} \Omega d^3}, \quad (22)$$

$$\Pi = \frac{P_{\text{turb}}}{\rho_{\text{in}} \Omega^3 d^5}, \quad (23)$$

$$\eta_{\text{turb}} = \frac{\Pi}{\Phi\Psi}, \quad (24)$$

where Ψ is the dimensionless pressure head, Φ is the dimensionless flow rate, Π is the dimensionless power coefficient, η_{turb} is the turbine efficiency, Ω is the turbine rotational speed (in radians per unit time), d is the turbine rotor diameter and ρ_{in} is a reference density defined in stagnation conditions at the turbine entrance. In equation (23), P_{turb} is the turbine aerodynamic power. The pneumatic power is defined as the power available for the turbine and is represented by P_{pneu} . The reference density was defined as

$$\rho_{\text{in}} = \begin{cases} \rho_c, & \text{if } p \geq p_{\text{at}} \text{ (exhalation)} \\ \rho_{\text{at}}, & \text{if } p < p_{\text{at}} \text{ (inhalation)} \end{cases}, \quad (25)$$

where ρ_c is the air density inside the air chamber and ρ_{at} is the atmospheric density.

Neglecting the effects of the variations in Reynolds number and Mach number [3], the dimensionless variables Φ , Π and η_{turb} can be plotted as simple curves as function of Ψ , as shown in Figure 3. The non-dimensional performance curves of the biradial turbine were obtained from model testing [10].

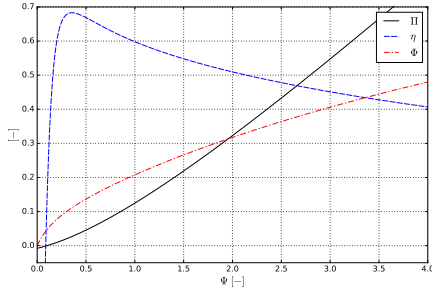


Figure 3: Dimensionless flow rate Φ , dimensionless power coefficient Π and efficiency η as functions of dimensionless pressure head Ψ , for the biradial turbine used in the numerical simulations. Retrieved from [10].

The instantaneous turbine aerodynamic torque was calculated from equations (23) and (24)

$$T_{\text{turb}} = \rho_{\text{in}} \Omega^2 d^5 \Pi. \quad (26)$$

The specific enthalpy at the turbine's outlet is defined as

$$h_{\text{turb}}^{\text{out}} = \begin{cases} h_c - \left(\frac{p - p_{\text{at}}}{\rho_{\text{in}}} \right) \eta_{\text{turb}}, & \text{if } p \geq p_{\text{at}} \\ & \text{(exhalation)} \\ h_{\text{at}} + \left(\frac{p - p_{\text{at}}}{\rho_{\text{in}}} \right) \eta_{\text{turb}}, & \text{if } p < p_{\text{at}} \\ & \text{(inhalation)} \end{cases}, \quad (27)$$

where h_{at} is the atmospheric specific enthalpy.

2.4. Inertia of the rotating parts

The dynamics between the turbine and the generator was described in the inertia sub-model, as follows

$$I\dot{\Omega} = T_{\text{turb}} - T_{\text{gen}}^{\text{em}}, \quad (28)$$

where I is the moment of inertia and $T_{\text{gen}}^{\text{em}}$ is the instantaneous generator electromagnetic torque imposed by the rotational speed control law. The inertia was calculated through dimensional analysis using data from the biradial turbine installed within the H2020 OPERA project at the Mutriku power plant, which as a diameter of 0.50 m and a rotational inertia of 5.01 kg m² [10],

$$I = 5.01 \left(\frac{d}{0.5} \right)^5, \quad (29)$$

where d is the turbine rotor diameter.

2.5. Generator

The power performance of an OWC is strongly affected by the air turbine type and size, the control of the turbine rotational speed and the rated power of the generator. Several generator control laws have been proposed for OWCs. One of the most simple and effective control laws can be derived from simple physical arguments. Considering the limiting case when the inertia I tends to zero, equation (28) shows that the instantaneous turbine torque is equal to the instantaneous generator torque, thus, since torque is directly proportional to power $P = T\Omega$, the instantaneous turbine power is equal to the instantaneous generator power. If the turbine is to be operated close to the best efficiency point Ψ_{bep} , i.e., $\eta(\Psi_{\text{bep}}) \geq \eta(\Psi)$, then the turbine power is proportional to

$$P_{\text{turb}}(\Psi_{\text{bep}}, \Omega) = \underbrace{\rho_{\text{in}} d^5 \Pi_{\text{turb}}(\Psi_{\text{bep}})}_{a=\text{const}} \Omega^3, \quad (30)$$

and the generator electromagnetic power must follow the relation

$$P_{\text{gen}}^{\text{em}} = a\Omega^3. \quad (31)$$

Equation (31) shows that, in order to maximize the time-averaged turbine aerodynamic efficiency, the turbine output power should be proportional to Ω^3 .

The following control law was adopted in order to avoid overpowering the generator

$$P_{\text{gen}}^{\text{em}} = \min(P_{\text{gen}}^{\text{rated}}, a\Omega^3), \quad (32)$$

where $P_{\text{gen}}^{\text{rated}}$ is the rated (maximum allowed) power of the generator.

The generator electrical power output P_{elect} was computed as

$$P_{\text{elect}} = \eta_{\text{gen}}(\Lambda_{\text{gen}}) P_{\text{gen}}^{\text{em}}, \quad (33)$$

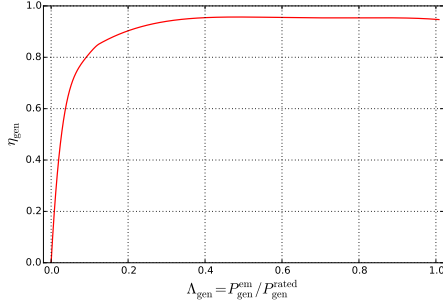


Figure 4: Generator efficiency curve. Retrieved from [3].

where η_{gen} is the generator efficiency and was retrieved from Figure 4 as the function of the generator load Λ_{gen} ,

$$\Lambda_{\text{gen}} = \frac{P_{\text{gen}}^{\text{em}}}{P_{\text{gen}}^{\text{rated}}}. \quad (34)$$

The instantaneous generator electromagnetic torque is expressed as

$$T_{\text{gen}}^{\text{em}} = P_{\text{gen}}^{\text{em}} \Omega^{-1}. \quad (35)$$

2.6. Atmosphere

The atmosphere works as a source of mass flow rate and constant pressure and enthalpy when the flow enters the turbine from the atmosphere, and as a sink when the flow exists the turbine to the atmosphere.

3. Results and discussion

The hydrodynamic model without the PTO was validated through the comparison of the obtained results with the ones obtained from a frequency domain model implemented in Mathematica. It was found that the buoy's displacement results were in good agreement with the ones obtained in the frequency domain.

A sensitivity analysis was performed to study the influence of the modification of the design variables on the power output of the BBDB. The performance of the WAVEBUOY was evaluated and modifications to its geometry were made in accordance with the results from the sensitivity analysis.

3.1. Sensitivity analysis

The variables studied in the sensitivity analysis were the buoy's width w , the transversal area of the duct defined as $A_{\text{transv}} = l_2 \times w = h_2 \times w$, in which is consequently varied both the buoy's length l and height h , and the length of the duct s (Figure 5). The ratio of the transversal area between the inlet of the duct and the cross section of the air chamber at the water level is kept constant in each modification, in order to avoid the acceleration and deceleration of the fluid, since the model

is not able to represent that behaviour. Both the length l_1 and height h_1 of the floater were kept constant. The variables w and A_{transv} were reduced by 50% and 25% and increased by 25%, 50%, 75% and 100% from their initial values and variable s was increased by 25%, 50%, 75% and 100% from the initial value of l_1 . The initial values of each variable are presented in Table 2.

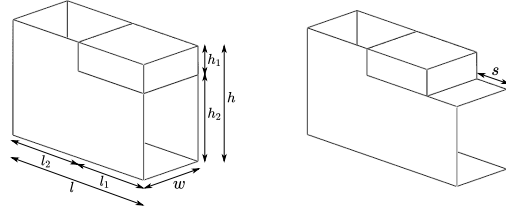


Figure 5: Representation of the variables studied in the sensitivity analysis.

Table 2: Initial values of each variable studied in the sensitivity analysis.

Variable	Reference value
l	6 m
h	4 m
w	2.5 m
h_1	1 m
h_2	3 m
l_1	3 m
l_2	3 m
s	0 m
A_{transv}	7.5 m ²

The hydrodynamic coefficients that serve as input to the numerical model were computed by WAMIT. The mesh was discretized using the high-order method. The BBDB geometry was defined using explicit analytical formulae coded in FORTRAN, modifying the GEOMXACT library and generating a dynamic link library that WAMIT was able to read. The criteria used to specify the mesh element size were based on [11], where it was used a mesh whose resolution is dependent on the device size and on the wavelength of the incident wave. A convergence analysis of the hydrodynamic parameters was performed in order to select an adequate mesh discretization.

The power output of each buoy was estimated through the numerical model, considering a fixed turbine diameter of 0.316 m. The performance is quantified in terms of capture width ratio (CWR)

$$\text{CWR} = \frac{\bar{P}_{\text{turb,ann}}}{\bar{P}_{\text{wave,ann}} L}, \quad (36)$$

where $\bar{P}_{\text{turb,ann}}$ is the annual average wave power absorbed by the turbine that is computed by equation (23) for the wave climate referred in section 2.1. The annual average flux of energy transported by the waves is denoted by $\bar{P}_{\text{wave,ann}}$ and L represents the characteristic length, in this case the buoy's width. Figures 6-8 present the CWR for the variations of width, transversal area and duct extent, respectively, for two incident wave angles β .

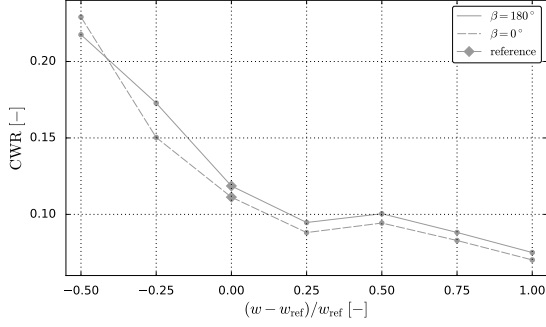


Figure 6: Variation of the capture width ratio with the buoy's width for two incident wave angles.

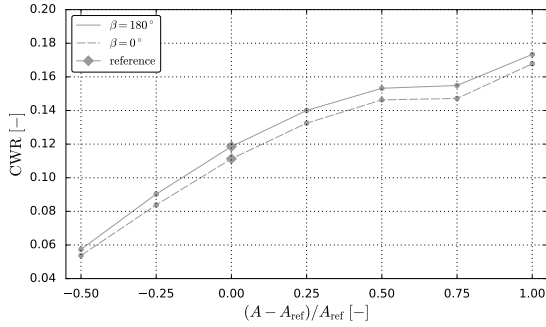


Figure 7: Variation of the capture width ratio with the buoy's transversal area for two incident wave angles.

Figures 6-8 show that, in general, when the devices are subjected to an incident wave angle of 180 degrees, have a better performance, which is coherent with the literature [12]. However, the difference between the values of 0 and 180 degrees is not significant, being the average difference of about 6.50%, leading to the conclusion that the power output is independent of the wave heading. The evolution of CWR is inversely proportional to the width's variation, as observed in Figure 6. From Figure 7, one can see that the CWR curves are directly proportional to the transversal area. Figure 8 shows the evolution of CWR in function of the duct extent. It is observed that the CWR increases with the duct extension until a certain point, from which it begins to decrease. This is consistent with what is

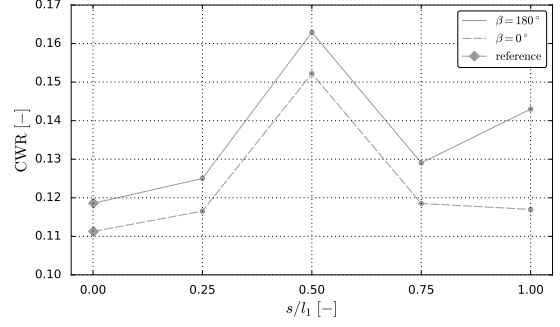


Figure 8: Variation of the capture width ratio with the buoy's duct extension for two incident wave angles.

found in [13], where experimental tests show that longer ducts may not necessarily improve the efficiency. Overall, geometries with a smaller width, larger transversal area or longer ducts presented a great influence on the CWR. It can be concluded that these alterations to the reference geometry lead to an improvement of the buoy's performance. It is important to note that the turbine diameter was imposed, therefore the turbine diameter is not the adequate for each buoy, which justifies the non uniform behaviour of the CWR curves.

3.2. Performance assessment of the WAVEBUOY

The criteria used to specify the size of the mesh used in WAMIT was the same as in section 3.1. The subroutine with the explicit analytical formulae coded in FORTRAN, and incorporated in the GEOMXACT dynamic linked library to be read by WAMIT, used to generate the mesh needed to be adapted from the previous basic BBDB geometry to the WAVEBUOY geometry. A mesh with 8330 panels was used and is depicted in Figure 9.

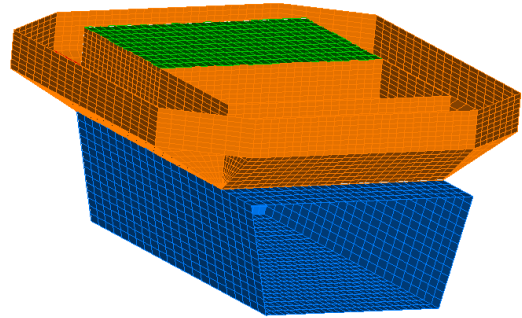
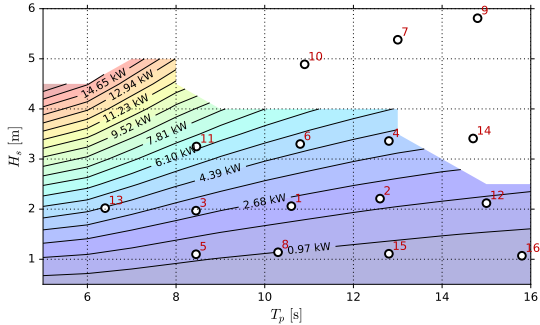


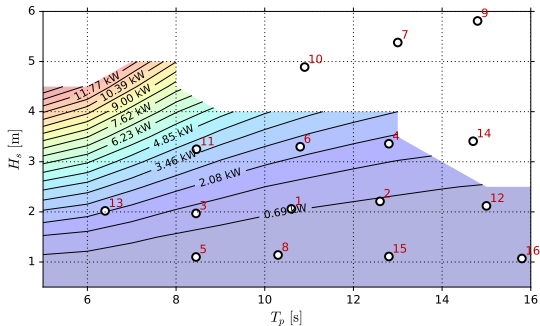
Figure 9: WAVEBUOY's submerged surface geometry modelled in WAMIT.

The power output of the WAVEBUOY was estimated through the time domain model for the

Azores' wave climate, considering a fixed diameter of 0.316 m, specified by the project. The sensitivity of the turbine and electric power as function of the significant wave height and peak period, for incident wave angles of 180 degrees, is depicted in Figure 10.



(a) Turbine shaft power matrix.



(b) Electric power matrix.

Figure 10: Power matrices for the WAVEBUOY original design for an incident wave angle of 180 degrees.

From Figure 10, it can be seen that the buoy does not perform in some sea states, the ones presented in the blank area. In these cases, the OWC reaches the turbine and it stops working. In order to try to increase the buoy's availability, and to improve the buoy's performance, some modifications to the geometry were made. According to the sensitivity analysis, smaller widths, larger transversal areas and longer ducts provide better performance. Due to some project restrictions, it was decided to only change the length of the extended duct.

3.3. Performance assessment with different duct lengths

With the objective of improving the performance of the WAVEBUOY, the length of the duct was increased by 1 m and 2 m. Studies were performed for buoys with a length of 5 m and 6 m. Further extensions of the duct were not considered because the buoy has to be as small as possible, due to costs, structural and transport considerations. The comparison between the mean turbine, P_{turb} , and electric powers, P_{elect} , CWR and availability α , which

is the sum of the probability of occurrence of the sea states for which the buoys work, is presented in Table 3, for the three buoys studied.

Table 3: Variation of the mean turbine and electric powers [W], capture width ratio and availability [%] in function of the buoy's length [m].

Length	P_{turb}	P_{elect}	CWR	α
4	2285	866	0.096	87
5	2719	1311	0.115	66
6	1502	412	0.063	97

Table 3 shows that the 5 m buoy generates more power, although has a lower availability. On the other hand, the 6 m long buoy, produces less power but presents a higher availability. Since the low availability is associated with the OWC reaching the turbine, a higher air chamber could solve the problem. The poor performance can be explained by the turbine rotor diameter not being optimum for energy extraction. With that in mind, first, it was studied the variation of the turbine rotor diameter, and then, the increase of the height of the air chamber.

3.4. Performance assessment with different turbine rotor diameters

The buoys that presented the highest CWR and availability were the ones chosen to conduct the study of the variation of the turbine's rotor diameter, i.e., the buoys with lengths of 5 m and 6 m, respectively. The buoy's performance was evaluated for five different diameters: 0.25 m, 0.275 m, 0.316 m, 0.325 m and 0.35 m. Tables 4 and 5 show the mean values of turbine and electric powers, CWR and availability in function of the turbine's diameter for the buoys with 5 m and 6 m length, respectively.

Table 4: Variation of the mean turbine and electric powers [W], capture width ratio and availability [%] in function of the buoy's diameter [m] for a buoy of 5 m.

Diameter	P_{turb}	P_{elect}	CWR	α
0.250	2450	1043	0.103	79
0.275	2783	1310	0.117	77
0.316	2719	1311	0.115	66
0.325	2318	1155	0.098	54
0.350	1297	684	0.055	29

From Tables 4 and 5, it is observed that, the increase of the diameter improves the buoys' performance, until a certain diameter, which should be close to the optimal turbine rotor diameter for the geometry, but decreases the device's availability. Due to the fact that the buoy needs to provide continuous real-time data measurements, an

Table 5: Variation of the mean turbine and electric powers [W], capture width ratio and availability [%] in function of the buoy’s diameter [m] for a buoy of 6 m.

Diameter	P_{turb}	P_{elect}	CWR	α
0.250	1069	225	0.045	100
0.275	1260	300	0.053	100
0.316	1502	412	0.063	97
0.325	1573	445	0.066	97
0.350	1386	356	0.058	89

availability of 100% is desired. For the buoy of 6 m that value of availability is attained for diameters of 0.25 m and 0.275 m, however the electric power generated by those buoys is below the minimum range of 300-500 W that is needed to feed the oceanographic instruments. On the other hand, the buoy of 5 m produces a great amount of electric power, but has a maximum value of availability of only 79%. Since the low availability is due to the OWC reaching the turbine, simulations considering a higher air chamber were conducted.

3.5. Performance assessment with a different air chamber height

The original WAVEBUOY design considers an air chamber with a height of 1.80 m. In this study, an air chamber with a height of 2.80 m, i.e., a chamber one meter higher than the original WAVEBUOY design, is evaluated. Tables 6 and 7 present the mean values of turbine and electric powers, CWR and availability in function of the turbine’s diameter for the buoys with 5 m and 6 m length, respectively, for an air chamber with a height of 2.80 m.

Table 6: Variation of the mean turbine and electric powers [W], capture width ratio and availability [%] in function of the buoy’s diameter [m] for a buoy of 5 m and an air chamber with a height of 2.80 m.

Diameter	P_{turb}	P_{elect}	CWR	α
0.250	4010	2053	0.169	100
0.275	4505	2442	0.190	97
0.316	4929	2805	0.208	91
0.325	4629	2595	0.195	87
0.350	5303	3148	0.223	87

Analysing the results from Tables 6 and 7, both the buoys’ performance and availability increased considerably compared to the buoys with an air chamber with a height of 1.80 m.

The average turbine power increases with the chamber height increase. If the air chamber is small, the air flow is almost incompressible and the phase difference between the OWC motion and the buoy motion is almost negligible. A larger chamber increases the spring effect resulting from air compress-

Table 7: Variation of the mean turbine and electric powers [W], capture width ratio and availability [%] in function of the buoy’s diameter [m] for a buoy of 6 m and an air chamber with a height of 2.80 m.

Diameter	P_{turb}	P_{elect}	CWR	α
0.250	1069	225	0.045	100
0.275	1259	300	0.053	100
0.316	1591	449	0.067	100
0.325	1666	485	0.070	100
0.350	1882	595	0.079	100

ibility (less stiff system) and increases the phase angle of the OWC motion with respect to the buoy heave motion. In this case, the relative displacement of the buoy with respect to the OWC is larger.

3.6. Proposed WAVEBUOY modification

The proposed WAVEBUOY should have the smallest geometry possible that generates the highest power output, hence smaller geometries are less expensive and easier to transport. It should also present an availability of 100%, in order to provide continuous real-time data measurements. The buoy that fulfils those requirements is the one with a length of 5 m, an air chamber with a height of 2.80 m and a turbine rotor diameter of 0.25 m. It has a mean electric power output of 2053 W, which is much higher than the required range of 300-500 W that is needed to feed the oceanographic instrumentation. It was observed that the buoy is capable of producing 300-500 W during almost all sea states, corresponding to a total probability of occurrence of 91%. Table 8 shows a comparison of the mean turbine and electric powers, capture width ratio and availability between the original and the proposed WAVEBUOY designs. From Table 8, it is clear that the proposed geometry improves considerably the buoy’s performance and availability.

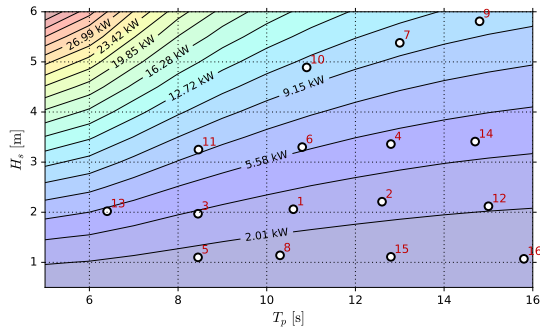
Table 8: Comparison of the mean turbine and electric powers [W], capture width ratio and availability [%] between the original and the proposed WAVEBUOY designs.

Design	P_{turb}	P_{elect}	CWR	α
Original	2285	866	0.096	87
Proposed	4010	2053	0.169	100

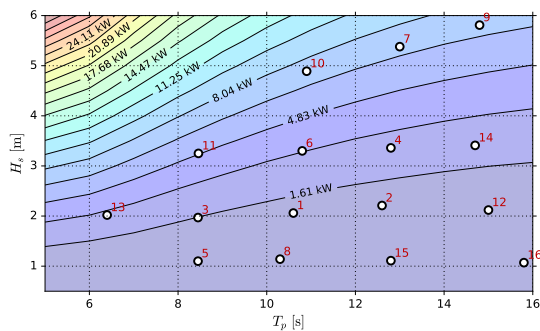
Figure 11 shows the sensitivity of the turbine and electric power as function of the significant wave height and peak period, for an incident wave angle of 180 degrees, for the proposed WAVEBUOY.

4. Conclusions

From the sensitivity analysis performed to the basic BBDB geometry, it was observed that the power output was inversely proportional to the buoy’s



(a) Turbine shaft power matrix for the proposed WAVE-BUOY design.



(b) Electric power matrix for the proposed WAVEBUOY design.

Figure 11: Power matrices for the proposed WAVE-BUOY design for an incident wave angle of 180 degrees.

width, directly proportional to the buoy's transversal area and increased with extent of the duct until a certain length and then decreased.

From the performance evaluation of the WAVE-BUOY, it was observed that the buoy presented a low availability. Aiming to increase both the performance and the availability, some parameters were varied. First, the duct was elongated, next, the turbine rotor diameter was varied and last, the air chamber's height was increased. A buoy with a duct extension of 1 m, a height increase of the air chamber of 1 m and a smaller turbine rotor diameter of 0.25 m produced 2053 W and presented a power availability of 100%, which is more 1187 W and 13% than the original design.

References

[1] M. Suzuki, T. Kuboki, S. Nagata, and T. Setoguchi. Numerical investigation of 2D optimal profile of backward-bent duct type wave energy converter. In *ASME International Conference on Ocean, Offshore and Arctic Engineering*, volume 4, pages 973–982, 2009. doi:10.1115/OMAE2009-79719.

[2] J. C. C. Portillo, J. C. C. Henriques, and L. M. C. Gato. Mathematical modelling for the degrees of freedom of the oscillating water column. Internal

Report, Instituto Superior Técnico, May 2018.

[3] J. C. C. Henriques, J. C. C. Portillo, L. M. C. Gato, R. P. F. Gomes, D. N. Ferreira, and A. F. O. Falcão. Design of oscillating-water-column wave energy converters with an application to self-powered sensor buoys. *Energy*, 112:852–867, October 2016. doi.org/10.1016/j.energy.2016.06.054.

[4] J. C. C. Henriques, M. F. P. Lopes, R. F. P. Gomes, L. M. C. Gato, and A. F. O. Falcão. Performance evaluation of a two-body heaving WEC with latching control using a new numerical method. In *Proceedings of the 9th European Wave and Tidal Energy Conference*, September 2011.

[5] R. P. F. Gomes. *Wave energy extraction from oscillating systems: numerical modelling and experimental testing*. PhD thesis, Instituto Superior Técnico, 2013.

[6] P. Ribeiro, J. C. C. Henriques, and L. M. C. Gato. Wave climate characterization of Azores for the WAVEBUOY project. Internal Report, Instituto Superior Técnico, May 2018.

[7] M. Alves. *Handbook of Ocean Wave Energy*, chapter Wave-to-Wire Modelling of WECs, pages 261–287. Springer International Publishing AG, December 2016.

[8] National Renewable Energy Laboratory and Sandia National Laboratories. Boundary element method input/output (BEMIO) documentation and users guide, wec-sim.github.io/bemio/, Accessed in 7th April 2018.

[9] J. C. C. Portillo, J. C. C. Henriques, L. M. C. Gato, R. P. F. Gomes, and A. F. O. Falcão. Performance assessment of a floating coaxial ducted OWC wave energy converter for oceanographic purposes. In *Proceedings of the ASME 2015 34th International Conference on Ocean, Offshore and Arctic Engineering*, May 2015. doi:10.1115/OMAE2015-41975.

[10] L. M. C. Gato, A. A. D. Carrelhas, F. X. C. Fonseca, and J. C. C. Henriques. Turbine-generator set laboratory tests in variable unidirectional flow. Technical report, Instituto Superior Técnico, June 2017. Available at: opera-h2020.eu/wp-content/uploads/2016/03/OPERA-D3-2-Dry-Testing-IST.pdf.

[11] L. Sjökvist, M. Göteman, M. Rahm, R. Waters, O. Svensson, E. Strömstedt, and M. Leijon. Calculating buoy response for a wave energy converter — A comparison of two computational methods and experimental results. *Theoretical and Applied Mechanics Letters*, 7(3):164–168, May 2017. doi.org/10.1016/j.taml.2017.05.004.

[12] Y. Masuda, T. Yamazaki, Y. Outa, and M. E. McCormick. Study of backward bent duct buoy. In *OCEANS '87*, November 1987. doi.org/10.1109/OCEANS.1987.1160750.

[13] B. B. Baanu, B. V. Mudgal, and P. Jalihal. Experimental investigations on performance characteristics of duct extended models of backward bent duct buoy (bbdb). *Imperial Journal of Interdisciplinary Research*, 2(5):1838–1843, 2016.